PAPER

Check for updates

The adsorption properties and mechanisms of magnetic carbon–silicon composites *in situ* prepared from coal gasification fine slag†

Chenxu Sun, Haoqi Pan, Tingting Shen, [ID] * Jing Sun,* Shaocang He, Tianpeng Li and Xuqian Lu

A novel magnetic carbon–silicon composite (Fe-HH-CGFS) was prepared from solid waste coal gasification fine slag (CGFS) by a two-step acid leaching and one-step chemical co-precipitation process, which was optimized using a 3-factor, 3-level Box–Behnken design and then analyzed for correlation. Fe-HH-CGFS was characterized by scanning electron microscopy (SEM), X-ray diffraction (XRD), X-ray photoelectron spectroscopy (XPS), Brunauer–Emmett–Teller (BET), thermal gravimetric analysis (TGA), and vibrating sample magnetometer (VSM) measurements. The results demonstrated that Fe-HH-CGFS had a reverse spinel structure with an average particle size of 5.14 nm, exhibiting a microporous/mesoporous structure with a specific surface area (SSA) of 196.84 m^2 g^{-1} and pore volume of 0.346 cm^3 g^{-1}. Furthermore, Fe-HH-CGFS could achieve 97.59% removal efficiency of rhodamine B (RhB) under the optimal conditions: an initial concentration of RhB of 100 mg L^{-1}, an adsorption time of 60 min, and a dosage of Fe-HH-CGFS of 1.0 g L^{-1}. The pseudo-second-order model and the Langmuir isotherm satisfactorily described the adsorption behavior. The results indicated that the RhB removal process was a single-molecule layer endothermic adsorption, which is dominated by chemical adsorption reactions. This work is expected to provide an alternative route for the high-value utilization of CGFS and offer a valuable insight for the recycling of other solid wastes, aligning with the green development concept of "treating wastes with wastes".

1. Introduction

Coal energy is one of the three major global energy sources. The clean and efficient utilization of coal resources can effectively alleviate the problem of tight supply and demand in the global energy market, which is crucial for ensuring sustainable economic development worldwide. Coal gasification technology is a highly efficient and environmentally friendly method.[1] At elevated temperatures, coal reacts with either oxygen or water vapor to generate gaseous byproducts including CO, H_2, and CH_4.[2] A significant quantity of coal gasification slag (CGS) is produced during this process, with an annual output of approximately 35 million tons in China alone.[3] Currently, most of this waste is landfilled and deposited in open areas, which not only takes up a lot of land resources but also puts a lot of pressure on environmental management. Therefore, the recycling of CGS has become a prominent research topic. CGS can be classified into two types: coal gasification coarse slag (CGCS) and coal gasification fine slag (CGFS).[4,5] CGFS possesses a favorable pore structure and a high residual carbon content (15–50%),[6,7] which lays a solid foundation for its application as a raw material in the preparation of functional materials.[8,9]

With adsorption being a more effective and economical method for treating wastewater,[10,11] CGFS has been utilized to fabricate three-dimensional porous zeolite-based composite materials,[12] novel porous adsorption materials (PAMs),[13] high-performance hierarchical porous composites (HPCs),[14] ferric sulfate modified carbon/zeolite composites[15] or carbon–silicon mesoporous composites with exceptional SSA and pore volume.[16] However, previous research has revealed that CGFS contains various metal oxides, which partly impede its utilization as a source of absorbents.[17]

Therefore, in this work, a novel approach is reported for the *in situ* synthesis of magnetic carbon–silicon composites based on CGFS through a two-step acid leaching process and a one-step chemical co-precipitation method. Firstly, the two-step acid leaching was initiated to erode out the metal oxides in CGFS to improve the microporous or mesoporous structure, and then the one-step chemical co-precipitation method was used to modify its magnetic performance, which was evaluated by the removal of RhB, a model indicator and a prevalent

School of Environmental Science and Engineering, Qilu University of Technology (Shandong Academy of Sciences), Jinan 250353, P. R. China. E-mail: shentingting@qlu.edu.cn; sunjing77@qlu.edu.cn

triphenylmethane dye found in printing and dyeing wastewater.[18–21] Furthermore, the resulting adsorbent was characterized by SEM, XRD, XPS, BET, TGA, and VSM. Additionally, the adsorption mechanisms, including adsorption kinetics and adsorption isotherms, were further investigated to reveal the adsorption process. This work is expected to provide an alternative route for the high-value utilization of CGFS and offer a valuable insight for the recycling of other solid wastes, aligning with the green development concept of "treating wastes with wastes".

2. Materials and methods

2.1 Materials

CGFS was supplied by Yankuang National Engineering Research Center of Coal Water Slurry Gasification and Coal Chemical Industry Co., Ltd. After the process of grinding and screening, CGFS with a particle size smaller than 150 μm was obtained. HCl and H_2SO_4 used in the experiments were purchased from Yantai Far East Technology Co., Ltd. HNO_3 was purchased from Sinopharm Chemical Reagent Co., Ltd. NaOH was purchased from Xilong Science Co., Ltd. $FeCl_2 \cdot 4H_2O$ was purchased from Shanghai Wokai Biotechnology Co., Ltd. $FeCl_3 \cdot 6H_2O$ was purchased from Tianjin Comio Chemical Reagent Co., Ltd. The water utilized in the experiments was deionized. Table 1 shows the elemental composition of the CGFS used in this experiment.

2.2 Methods

2.2.1 Two-step acid leaching process. The sieved and ground CGFS was continuously stirred at different temperatures (20, 25, 40, 60, and 80 °C), solid–liquid ratios (g : mL; 1 : 5, 1 : 10, 1 : 20, 1 : 30, and 1 : 40), concentrations (1.0, 2.0, 3.0, 4.0, and 5.0 mol L^{-1}) of HCl solution, and times (0.5, 1.0, 3.0, 5.0, and 7.0 h) using a digital thermostatic magnetic stirrer (85-2 Shanghai Shuangjie Experimental Equipment Co., Ltd) at the same speed. Filtration of the solids, which were then washed to neutral by deionized water, was performed using a Büchner funnel with medium-speed filter paper. The samples were dried in a blast oven at 95 °C for 8 h, followed by repeating the aforementioned procedure with HCl, HNO_3, H_2SO_4, and CH_3COOH, respectively. Based on the above two-step acid leaching process, the resulting carbon–silicon composites were named HH-CGFS (HCl, HCl), HN-CGFS (HCl, HNO_3), HS-CGFS (HCl, H_2SO_4), and HC-CGFS (HCl, CH_3COOH).

The leaching rate of CGFS (R_L) by acid treatment with different temperatures, concentrations, solid–liquid ratios, and times is expressed in eqn (1):

$$R_L = \frac{m_e - m_0}{m_L} \tag{1}$$

where R_L represents the leaching rate of CGFS, m_e (g) represents the weight of the resulting HH-CGFS and the dried filter paper plus residual sample, m_0 (g) represents the weight of the initial filter paper, and m_L (g) represents the initial CGFS weight.

2.2.2 One-step chemical co-precipitation process. The optimum carbon–silicon composite (HH-CGFS) produced after two-step acid leaching was further modified by a one-step chemical co-precipitation process. The dosage of HH-CGFS with a mixed solution of Fe^{3+} and Fe^{2+} was designed as 1 : 40 (g : mL). HH-CGFS was stirred with the Fe^{3+} and Fe^{2+} mixed solution at specific temperatures (20, 25, 40, and 60 °C), times (1.0, 2.0, 4.0, and 8.0 h), and molar ratios of Fe^{3+} to Fe^{2+} (2 : 1, 1 : 1, 1 : 2, and 2 : 3). After stirring, the pH was adjusted to the indicated pH values (9.0, 10.0, 11.0, and 12.0) with 4.0 mol L^{-1} NaOH solution and then the samples were slowly stirred for 40 min. The resulting magnetic carbon–silicon composites were then washed several times with deionized water to neutral, separated from the solid–liquid phase using a Büchner funnel with medium-speed filter paper and dried in a vacuum oven at 95 °C for 8 h before use. A schematic diagram illustrating the preparation route is presented in Scheme 1.

2.3 Response surface experimental design

Box–Behnken design (BBD) is a type of response surface methodology (RSM) commonly used in experimental design. By fitting a second-order polynomial equation model to the response surface and the experimental factors, it is possible to analyze correlations between each factor and the response value in the context of complex interactions.[22–24] This BBD design (Table S1†) was used to explore the effects of temperature (A), the molar ratio of $Fe^{3+} : Fe^{2+}$ (B), and pH (C) on the adsorption performance of Fe-HH-CGFS. BBD was designed using Design Expert 12, and a total of 17 experiments were conducted. And the RhB solution adsorption experiments were subjected to analysis of variance (ANOVA).

2.4 Performance investigations

The adsorption process was conducted in 200 mL simulated wastewater at 25 °C with stirring at a speed of 180 rpm for 1.0 h. The operational conditions were optimized by Fe-HH-CGFS dosage (0.1, 0.2, 0.5, 1.0, and 2.0 g L^{-1}), initial RhB concentration (50, 75, 100, 150, and 200 mg L^{-1}), and pH (3.0, 5.0, 7.0, 9.0, and 11.0). After adsorption for a specific time, the supernatant was immediately taken by a syringe, and the absorbance of the supernatant was measured at 554 nm by a UV spectrophotometer to calculate the concentration of the solution samples, and the removal efficiency (R_e) and adsorptive capacity (Q_e) were calculated using eqn (2) and (3), respectively.
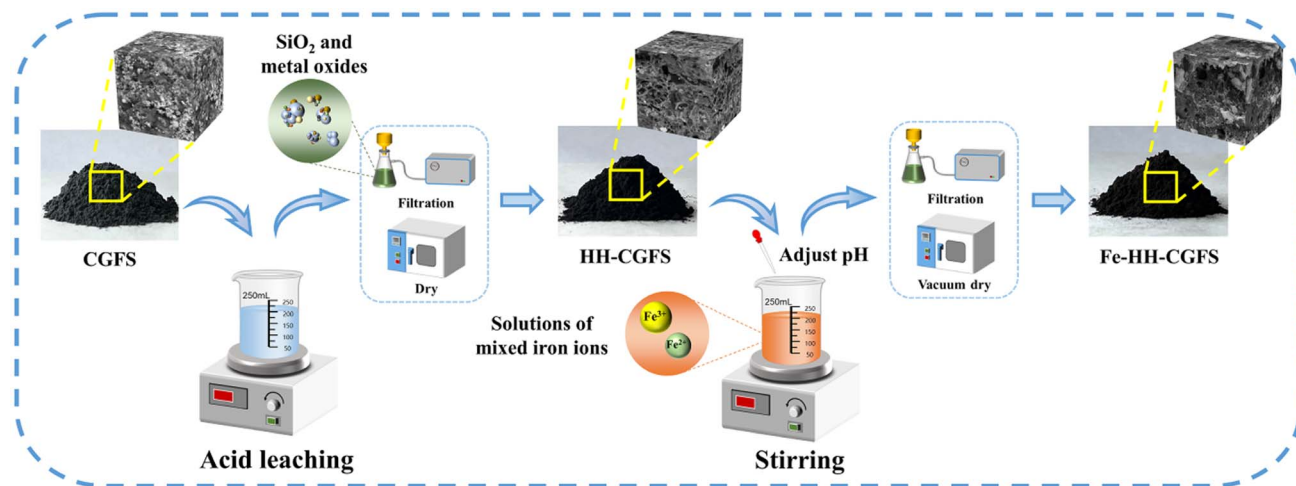
$$R_e = \frac{(C_0 - C_e)}{C_0} \times 100\% \tag{2}$$

$$Q_e = \frac{V \times (C_0 - C_e)}{W} \tag{3}$$

Table 1 The major elements of CGFS (wt%)^a

Elements	Si	Al	Fe	Ca	Na	Mg	K	Ti	LOI
CGFS	14.31	7.52	10.22	5.53	3.45	0.61	0.85	0.41	16.42

^{a} LOI: loss on ignition.

Scheme 1 Schematic diagram of the preparation route of Fe-HH-CGFS.

where C_0 (mg L^{-1}) and C_e (mg L^{-1}) are the concentrations of RhB wastewater at the beginning and equilibrium, respectively; V (L) is the volume of RhB wastewater; and W (g) is the weight of functional adsorbent added to the solution.

Furthermore, at the end of the adsorption process, the adsorbent was magnetically separated from the wastewater and then regenerated by NaOH. The Fe-HH-CGFS was magnetically separated, washed with distilled water, and then dried for use. This process of adsorption/desorption cycling was repeated five times to evaluate its stability.

2.5 Adsorption mechanism investigation

2.5.1 Adsorption kinetics. The adsorption process of RhB by Fe-HH-CGFS was evaluated using the pseudo-first-order (PFO) (eqn (4)), pseudo-second-order (PSO) (eqn (5)), and Weber–Morris particle intra-particle diffusion model (eqn (6)). The resulting adsorption kinetic curves were plotted to confirm the validity of these models.

$$q_t = q_e(1 - e^{-k_1 t}) \tag{4}$$

$$q_t = \frac{k_2 q_e^2 t}{1 + k_2 q_e t} \tag{5}$$

$$q_t = k_{di} t^{\frac{1}{2}} + C_i \tag{6}$$

Among them, q_e and q_t (mg g^{-1}) are the adsorption amount of the adsorbent at the equilibrium time and the given time, respectively; t (min) is the reaction time; k_1 (min^{-1}) is the PFO adsorption rate constant; k_2 (g mg^{-1} min^{-1}) is the PSO adsorption rate constant; k_{di} (mg g^{-1} min^{-1}) is the rate constant of the Weber–Morris intra-particle diffusion model; and C_i (mg g^{-1}) is related to the boundary thickness.

2.5.2 Adsorption isotherms. The Langmuir (eqn (7)), Freundlich (eqn (8)), and Temkin (eqn (9)) models were conducted to evaluate the adsorption process.

$$q_e = \frac{q_m K_L C_e}{1 + K_L C_e} \tag{7}$$

$$q_e = K_F C_e^{\frac{1}{n}} \tag{8}$$

$$q_e = \frac{RT}{b} \ln(K_T C_e) \tag{9}$$

where K_L (L mg^{-1}), K_F (mg g^{-1}), and K_T (L mg^{-1}) are the Langmuir constant, Freundlich constant, and Temkin constant, respectively; $R = 8.314$ J mol^{-1} K^{-1} is the ideal gas constant; T (K) is the absolute temperature; q_m (mg g^{-1}) is the maximum adsorption amount; n is the Freundlich index; and b (J mol^{-1}) is the coefficient of thermal effect.

2.6 Characterization methods

The physico-chemical properties of the samples were determined by the following characterizations in this study: scanning electron microscopy (SEM), X-ray diffraction (XRD), X-ray photoelectron spectroscopy (XPS), Brunauer–Emmett–Teller (BET), thermal gravimetric analysis (TGA), and vibrating sample magnetometer (VSM) measurements. The detailed characterization methods are presented in Text S1.†

3. Results and discussion

3.1 Preparation of Fe-HH-CGCS

3.1.1 Optimization of the two-step acid leaching process. Firstly, HCl is utilized to eliminate various metal oxides, such as Al$_2$O$_3$, CaO, MgO, K$_2$O, and Na$_2$O, from CGFS in order to create microporous/mesoporous structures. Then, HNO$_3$, HCl, H$_2$SO$_4$, and CH$_3$COOH were used to further open the pore channels and increase the SSA of the samples, respectively.

From Fig. 1a, the adsorption performance of RhB follows the order of HH-CGFS > HN-CGFS > HS-CGFS > HC-CGFS. As shown in Fig. 1b, the original CGFS had unstable performance and low adsorption capacity. However, after undergoing the two-step acid leaching process, the adsorption performance and stability were significantly enhanced. Considering both
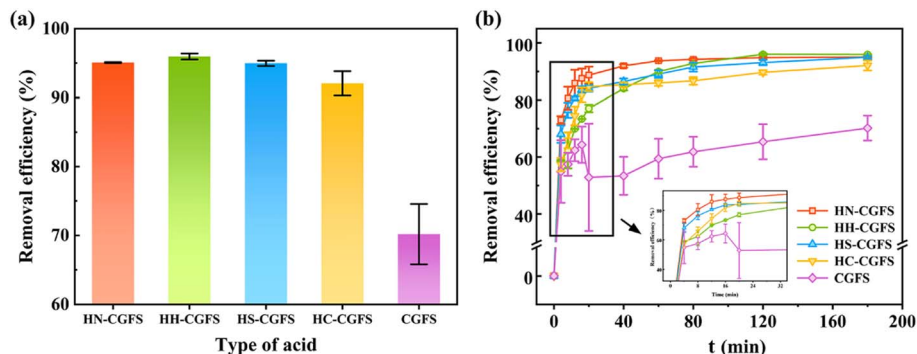
Fig. 1 Comparative investigations of the RhB removal efficiency by HN-CGFS, HH-CGFS, HS-CGFS, HC-CGFS, and CGFS. (a) Type of acid combination; (b) adsorption process.

material properties and cost, HCl was used for the two-step acid leaching process, and HH-CGFS was chosen for the following investigation.

Fig. 2a–d show the influence of the reaction temperature, solid–liquid ratio, acid concentration, and reaction time on the adsorption performance of HH-CGFS.

Fig. 2a demonstrates that the leaching efficiency of metal oxides and the removal efficiency of RhB increased gradually with the increase of the temperature at a range of 20 °C to 60 °C (64.93% to 73.00%). At the temperature of 60 °C during acid leaching, the increase was no longer observed. As the temperature mounted, the activity of the metal oxides in CGFS and the

rate of thermal movement of the molecules in solution increased, promoting a more vigorous reaction. When the temperature reached 80 °C, approaching the evaporation conditions of HCl, there was no further increase in the leaching efficiency of the metal oxides.[16] Fig. 2b indicated that the optimal treatment efficiency took place at the solid–liquid ratio of 1 : 20. The results revealed that the concentration of H+ in the solution is sufficient to react with the metal oxide in the CGFS, resulting in the formation of pore channels at the site where the original metal oxide was attached. Therefore, elevating the acid leaching temperature and solid–liquid ratio would be more conducive to the dissolution of metal oxides by HCl, thereby
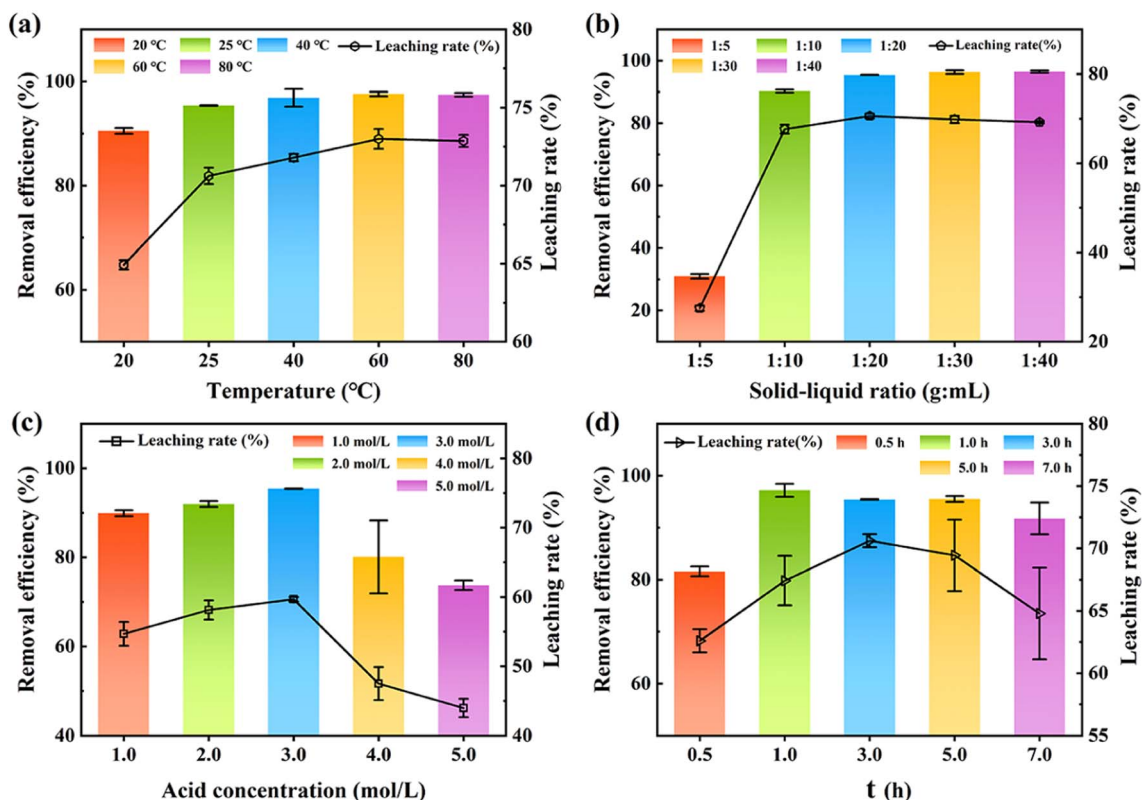

Fig. 2 The acid leaching rate of metal oxides and the removal efficiency of RhB by HH-CGFS under various conditions: (a) temperature, (b) solid–liquid ratio, (c) acid concentration, and (d) acid leaching time.

generating pore channels and providing additional adsorption sites for contaminants. Therefore, elevating the acid leaching temperature and solid–liquid ratio would be more conducive to the dissolution of metal oxides by HCl, thereby generating pore channels and providing additional adsorption sites for contaminants.[25,26]

Fig. 2c and d show that the leaching rate of HH-CGFS and the removal efficiency of RhB exhibited a bell-shaped trend with increasing acid concentration and acid leaching time. An excessive concentration of acid resulted in a decreased leaching rate of metal oxides due to the volatilization of HCl, and a too long acid leaching time increased the number of micropores in the CGFS, leading to a decrease in the average pore size.[27] Meanwhile, during the acid leaching process, the aluminosilicate phase might decompose into SiO_2 and $AlCl_3$ (eqn (10)).[13] These minute SiO_2 microspheres detach and persist within the pores, impeding further reaction of HCl with the metal oxides. Based on the above investigation and cost, the optimal conditions of HH-CGFS were selected as a solid–liquid ratio of 1 : 20, HCl concentration of 3.0 mol L^{-1}, acid leaching temperature of 60 °C, and acid leaching time of 1.0 h. Under the optimal conditions, the HH-CGFS adsorption capacity of RhB was up to 95.86 mg g^{-1}, and the R_L was 70.61%.

$$Al_2O_3 \cdot SiO_2 + 6HCl \rightarrow 2AlCl_3 + 3H_2O + SiO_2 \quad (10)$$

3.1.2 Optimization of the one-step chemical co-precipitation process. According to Fig. 3a and b, it was observed that increasing the stirring temperature above 40 °C and the stirring time beyond 1.0 h had a positive effect on enhancing the adsorption performance of Fe-HH-CGFS. Due to the thermal motion of solution molecules and surface tension, lower temperatures and shorter stirring time could cause droplet formation at the orifice opening and a series of cavities were left in the interior of HH-CGFS. The uneven filling of the HH-CGFS pores with Fe^{3+}/Fe^{2+} mixed solution led to significant agglomeration of the precipitate formed during the dropwise addition of NaOH solution, which impeded the uniformity of the Fe_3O_4 particles. This not only reduced the crystallinity of the magnetic Fe_3O_4 particles, but also significantly decreased the SSA and pore volume of Fe-HH-CGFS. Therefore, the conditions of continuous stirring and higher molecular thermal motion rates are more conducive to the formation of uniformly dispersed magnetic Fe_3O_4 particles with a reverse spinel structure.[28] Fig. 3c demonstrated that Fe-HH-CGFS exhibited superior removal efficiency and magnetic responsiveness to RhB when the molar ratio of $Fe^{3+} : Fe^{2+}$ was 1 : 1. This was attributed to the optimal molar ratio of $Fe^{3+} : Fe^{2+}$ ratio playing a great role in the formation of magnetic Fe_3O_4 particles of high purity, and the disproportionate molar ratio of $Fe^{3+} : Fe^{2+}$ might result in other types of iron oxides such as α-Fe_2O_3, α-FeO(OH), and $Fe_2O_3 \cdot 3H_2O$, inhibiting the formation of Fe_3O_4 particles.[29] The inserted photo in Fig. 3c also shows that the brownish-yellow color of the liquid may be attributed to the presence of $Fe_2O_3 \cdot 3H_2O$ particles, which were difficult to separate using a magnet due to their weak magnetic properties.
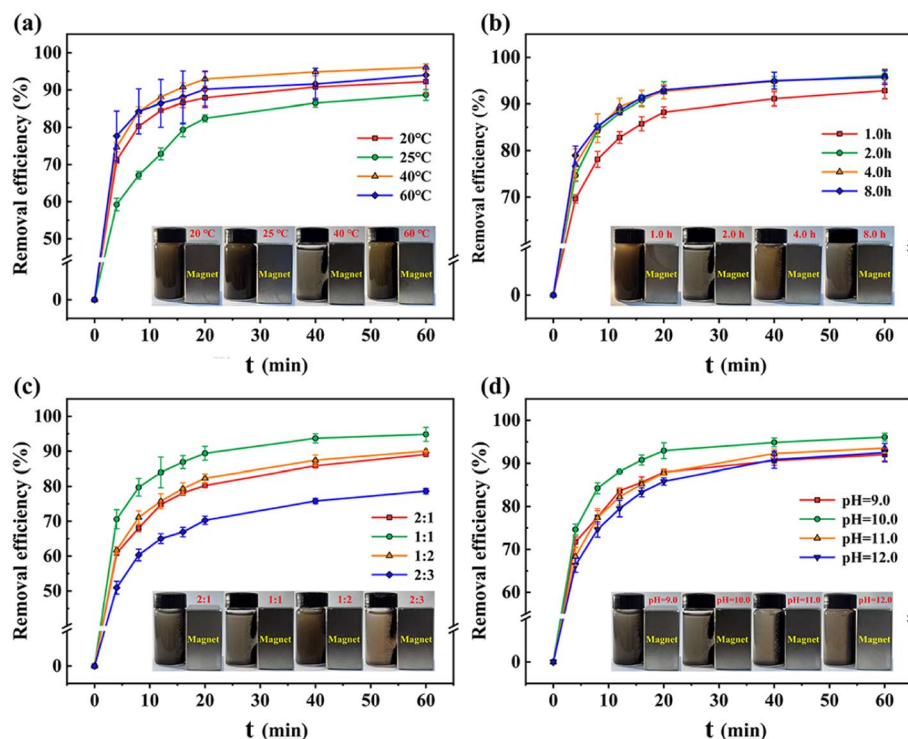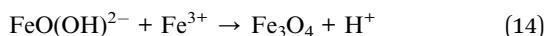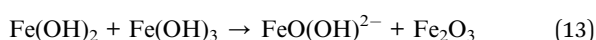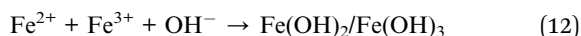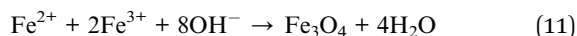

Fig. 3 Removal efficiency of RhB under various conditions: (a) temperature, (b) reaction time, (c) molar ratio of $Fe^{3+} : Fe^{2+}$, and (d) pH. Note: the magnetic responsiveness is presented in the inserted photos.

As shown in Fig. 3d, it was found that Fe-HH-CGFS exhibited superior performance at pH 10.0. The results demonstrated that pH played a great role in the formation of iron oxide species (Fe_3O_4, α-Fe_2O_3, α-$FeO(OH)$, and $Fe_2O_3 \cdot 3H_2O$) and the morphology of the magnetic Fe_3O_4 particles. At pH 9.0, the OH^- present in the solution was insufficient to facilitate the reaction from eqn (12) and (13) in the reaction mechanism.[30] Consequently, α-Fe_2O_3 (Hematite), which is formed by partial transformation of γ-Fe_2O_3 (Magnetic Hematite), is produced. This non-magnetic material not only occupies the pore channels, but also diminishes the magnetic reactivity of Fe-HH-CGFS. As the pH increased from 11.0 to 12.0, the removal efficiency of RhB decreased. Excessive OH^- might lead to the formation of $Fe(OH)_3$ and $Fe(OH)_2$, which inhibited the production of Fe_3O_4, decreasing the adsorption and magnetic properties of Fe-HH-CGFS. As the pH increased from 10.0 to 12.0, the removal efficiency of RhB decreased. As the particle size of the magnetic Fe_3O_4 formed during the reaction grew with pH,[29] which is detrimental to maintaining its high SSA and pore volume, when the pH increased from 10.0 to 12.0, the removal efficiency of Fe-HH-CGFS for RhB decreased. According to the reaction mechanism in eqn (14),[30] an excessive concentration of OH^- in the solution due to high pH will inhibit the formation of Fe_3O_4. The brownish-yellow colour of the water becomes more pronounced in the range of pH 11.0–12.0, as shown in the inserted photo in Fig. 3d.[31] In summary, the reaction temperature of 40 °C, stirring time of 2.0 h, molar ratio of $Fe^{3+}:Fe^{2+}$ of 1 : 1, and pH of 10.0 were determined as the optimal preparation conditions for Fe-HH-CGFS.

$$Fe^{2+} + 2Fe^{3+} + 8OH^- \rightarrow Fe_3O_4 + 4H_2O \tag{11}$$

$$Fe^{2+} + Fe^{3+} + OH^- \rightarrow Fe(OH)_2/Fe(OH)_3 \tag{12}$$

$$Fe(OH)_2 + Fe(OH)_3 \rightarrow FeO(OH)^{2-} + Fe_2O_3 \tag{13}$$

$$FeO(OH)^{2-} + Fe^{3+} \rightarrow Fe_3O_4 + H^+ \tag{14}$$

3.2 RSM investigations

3.2.1 BBD data analysis.
The effect of three independent variables (temperature, $Fe^{3+}:Fe^{2+}$, and pH) on the adsorption performance of RhB was investigated by analysis of BBD experimental data. The coded equation (eqn (15)) and the actual equation (eqn (16)) were obtained from Design-expert 12. The model equation based on the coded values was summed of 3 s-order factors, three interaction terms, three first-order factors, and a constant described as eqn (15) and (16). Furthermore, the coefficients can be used as indicators of the positive or negative impact on the response.

$$Y = 96.65 - 0.1013A - 6.42B - 0.1662C + 0.3550AB \\ + 0.4575AC + 1.12BC - 2.58A^2 - 8.80B^2 - 0.8503C^2 \tag{15}$$

$$R_e = 13.686 - 0.245737 \times \text{Temperature} - 33.862 \\ \times (Fe^{3+}:Fe^{2+}) - 13.69375 \times pH + 0.0355$$

$$\times \text{Temperature} \times (Fe^{3+}:Fe^{2+}) + 0.022875 \\ \times \text{Temperature} \times pH + 2.23 \times (Fe^{3+}:Fe^{2+}) \\ \times pH - 0.006438125 \times \text{Temperature}^2 - 35.211 \\ \times (Fe^{3+}:Fe^{2+})^2 - 0.85025 \times pH^2 \tag{16}$$

The actual and predicted RhB removal efficiency based on the Fe-HH-CGFS experimental design matrix are shown in Table S2.† ANOVA based on the lack of fit and Fisher's test (F-test) has been conducted to verify the significance and relevance of the reduced quadratic model summarized in Table S3.† The model's significance was adequately demonstrated by the F-value of 75.58, with a p-value less than 0.0001. The removal efficiency (Y) of RhB was significantly influenced by B and secondary B^2 ($P < 0.0001$), followed by A^2 ($P < 0.05$). The order of the effects of the three variables on the removal of RhB could be determined from the F-values as molar ratio of $Fe^{3+}:Fe^{2+}$ (B) > pH (C) > temperature (A).[32] In addition, the regression model had a high coefficient of determination ($R^2 = 0.9898$) and a difference between R_{adj}^2 and R^2 of less than 0.2 (Table S3†). It was found that the model can adequately describe the relationship between the response values and variables. The model achieved a reasonable accuracy of 23.0231 (Adeq Precision > 4), indicating a high level of model precision and good predictive confidence. Finally, the low coefficient of variation (CV = 1.12%) obtained in this study indicated that the model was stable and capable of predicting the optimal preparation conditions.[33]

3.2.2 3D response surface analysis.
Fig. 4a–c, obtained from the prediction model (eqn (15)), provided a more comprehensive visualization of the effect of the inter-factors on the response values. The results revealed that the optimization conditions were clear and unique, and each variable has a maximum value. The interaction between molar ratio of $Fe^{3+}:Fe^{2+}$ and temperature (Fig. 4a) was the most significant, followed by the interaction between molar ratio of $Fe^{3+}:Fe^{2+}$ and pH (Fig. 4b), and the interaction between pH and temperature (Fig. 4c) was the weakest. It is obvious that the removal efficiency of RhB shows a trend of increasing and then decreasing as the molar ratio of $Fe^{3+}:Fe^{2+}$ changes from 1 : 0.5 (2 : 1) to 1 : 1.5 (2 : 3), reaching a maximum near the molar ratio of $Fe^{3+}:Fe^{2+}$ = 1 : 1 (Fig. 4a and b). Additionally, Fig. 4c evidently shows that the interaction between pH and temperature is weak and has less effect on the removal efficiency of RhB. The change of these two factors causes a fluctuation of less than 4% in the RhB removal efficiency. Finally, it can be concluded that the molar ratio of $Fe^{3+}:Fe^{2+}$ has the most significant influence on the RhB removal rate, followed by pH and temperature. Therefore, it can be presumed that the molar ratio of $Fe^{3+}:Fe^{2+}$ is a key determinant of the morphology of the Fe_3O_4 particles.

3.3 Characterizations of Fe-HH-CGFS

3.3.1 SEM-EDS analysis.
Based on the SEM and EDS images presented in Fig. 5a–e, it is evident that alterations in the surface morphology of CGFS occurred as a result of both the two-step acid leaching method and the one-step chemical co-precipitation method. Fig. 5a illustrates the presence of
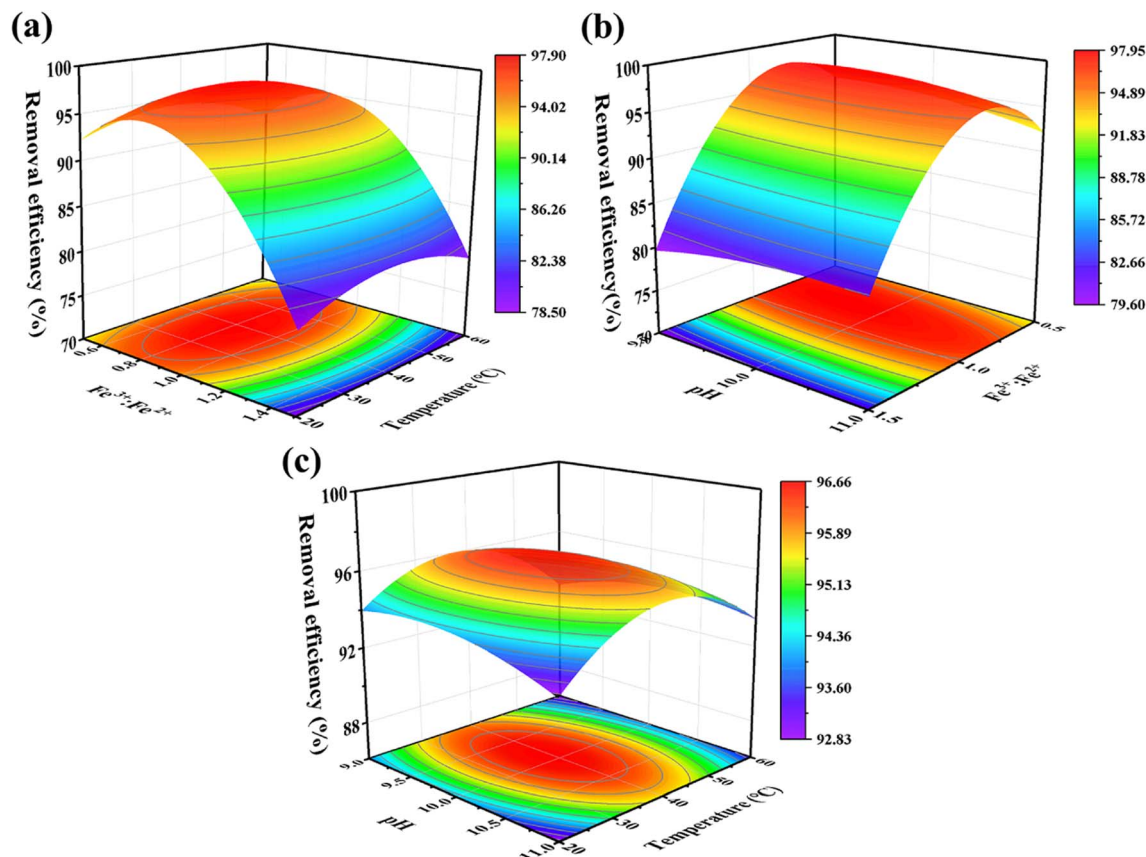
Fig. 4 The response surface plots showing the interaction of (a) molar ratio of $Fe^{3+} : Fe^{2+}$ and temperature, (b) pH and temperature, and (c) pH and molar ratio of $Fe^{3+} : Fe^{2+}$ on the RhB removal efficiency.

molten glass microspheres and metal oxides both on the surface and inside the pore channels of CGFS, which are crucial factors influencing its adsorption performance. As shown in Fig. 5b, the two-step acid leaching method resulted in a highly enriched porous structure of HH-CGFS. During the acid leaching process, H^+ continuously corrodes the metal oxides in the CGFS pore channels, further expanding the wedge-shaped pore channels inward and increasing both the pore volume and SSA based on a one-step acid leaching method.[27] The two-step acid leaching method effectively eliminated the metal oxides present in the CGFS, leaving a minimal amount of SiO_2 microspheres on the carbon skeleton. In this study, a porous material with a high C/Si ratio and reduced impurities was prepared using a two-step acid leaching method as opposed to a one-step acid leaching method.[25] As shown in Fig. 5c, the surface and pores of the porous carbon skeleton of Fe-HH-CGFS were loaded with Fe_3O_4 particles. These particles had rough and irregular surfaces. Importantly, the porous structure of the irregular unburned carbon also serves as an excellent deposition platform for magnetic particles and prevented the agglomeration of large particles. The Fe-HH-CGFS content could be determined through EDS spectroscopy analysis (Fig. 5d). Combined with the mapping images (Fig. 5e), it was evident that Fe, Si, and Al were uniformly distributed throughout the carbon skeleton, and the Fe_3O_4 particles exhibited minimal agglomeration and excellent

dispersion. This not only avoids excessive occupation of the original pore channels, but also creates rough Fe_3O_4 surfaces that provide additional adsorption sites.[34,35]

3.3.2 XRD analysis. As shown in Fig. 6a and b, it was found that CGFS and HH-CGFS had two obvious sharp peaks at $2\theta = 2$ 0.78° and 26.6° (Fig. 6a), corresponding to the characteristic peaks of SiO_2. Furthermore, the SiO_2 peaks of HH-CGFS showed a higher intensity after the removal of metal oxides by a two-step acid leaching method. The intensity of the SiO_2 peaks of Fe-HH-CGFS is slightly weakened by doping with Fe_3O_4. Moreover, the Fe-HH-CGFS peaks at $2\theta = 29.99°$, 35.30°, 39.89°, 53.78°, 57.5°, and 62.72° showed good agreement with the (220), (311), (400), (422), (511), and (440) planes of Fe_3O_4 nanoparticles (JCPDS card NO. 19-0629).[36–38] This indicated that the loaded Fe_3O_4 particles had a reverse spinel structure and that the quartz structure remained intact after Fe_3O_4 particle loading, which is of great importance.[39–42]

Due to the formation of other iron oxides, such as $\alpha\text{-}Fe_2O_3$, $\alpha\text{-}FeO(OH)$, and $Fe_2O_3\text{–}3H_2O$, the adsorbents prepared with different molar ratios of $Fe^{3+} : Fe^{2+}$ exhibited a reduction in the intensity of the SiO_2 peak and did not show the diffraction peak of Fe_3O_4 (Fig. 6b). Finally, the average crystallite size of the Fe_3O_4 particles in the Fe-HH-CGFS prepared at a molar ratio of $Fe^{3+} : Fe^{2+}$ of $1:1$ was calculated using the Debye–Scherrer equation (eqn (17)):[43]
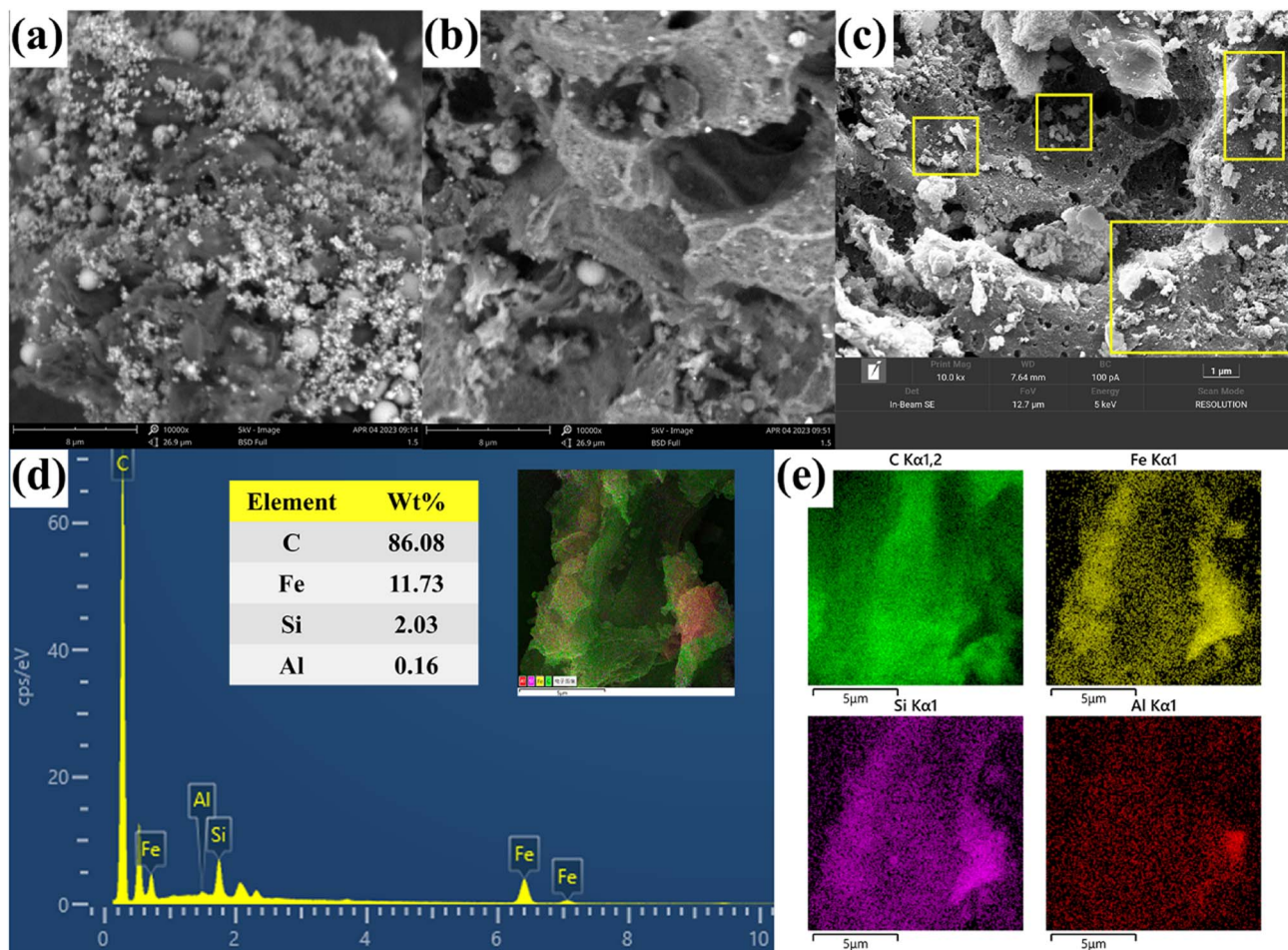
Fig. 5   SEM patterns of (a) CGFS, (b) HH-CGFS, and (c) Fe-HH-CGFS; and EDS elemental mapping of (d and e) Fe-HH-CGFS.
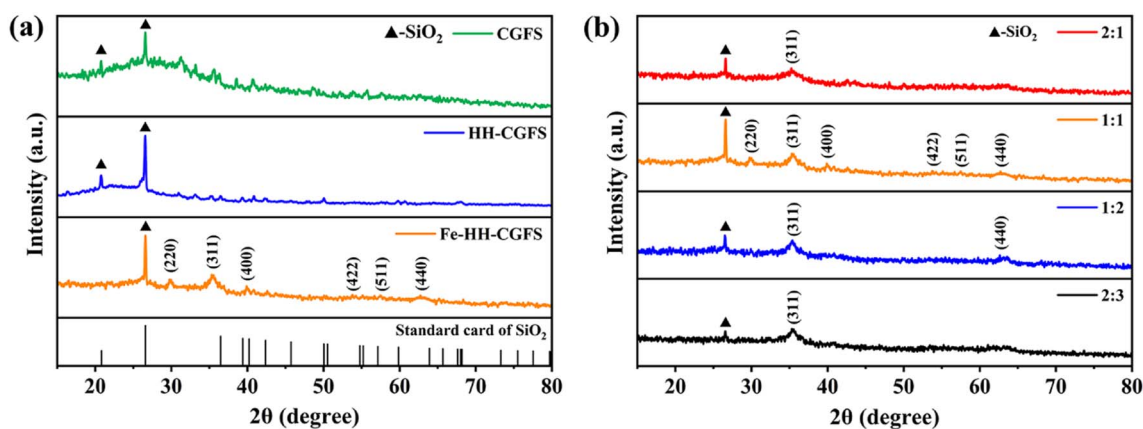

Fig. 6   XRD patterns: (a) CGFS, HH-CGFS, and Fe-HH-CGFS; (b) Fe-HH-CGFS prepared with various molar ratios of $Fe^{3+} : Fe^{2+}$.

$$D = \frac{K\lambda}{\beta \cos \theta} \qquad (17)$$

where D denotes the average size of the Fe_3O_4 nanoparticles, λ represents the X-ray wavelength (0.15418 nm), K refers to the Scherrer constant (0.9), β is the peak full width at half maximum (FWHM), and θ represents the Bragg diffraction angle. By

utilizing the most prominent (311) peak and its corresponding full width at half maximum in Fig. 6b, it was computed that the average size of the Fe_3O_4 particles was 5.14 nm, which is in the nanoscale range.

3.3.3 BET analysis. The N_2 adsorption–desorption isotherms and pore size distribution of CGFS, HH-CGFS, and

Fe-HH-CGFS were calculated by the DFT method. It can be seen from Fig. 7a that the adsorption–desorption isotherms of CGFS, HH-CGFS, and Fe-HH-CGFS showed the characteristics of type IV isotherms. The isotherms of CGFS and HH-CGFS showed H4 hysteresis at $P/P_0 > 0.4$, while those of Fe-HH-CGFS showed H3 hysteresis.[44] These results indicated that Fe-HH-CGFS had a complex microporous/mesoporous structure.[45–47] According to the pore size distribution curve (Fig. 7b), the majority of CGFS pores fall within the range of 0.72–2.00 nm, while HH-CGFS after two-step acid leaching exhibits a predominant pore size distribution in the range of 0.70–1.90 nm; on the other hand, Fe-HH-CGFS is characterized by mainly mesopores with $d >$ 3.20 nm. In addition, the SSA of CGFS increased from 52.59 m^2 g^{-1} to 230.31 m^2 g^{-1} after two-step acid leaching, but decreased slightly to 196.84 m^2 g^{-1} after loading Fe$_3$O$_4$ particles.

Importantly, the pore volume of CGFS was increased from 0.085 cm^3 g^{-1} to 0.218 cm^3 g^{-1} through a two-step acid leaching process and further enhanced to 0.346 cm^3 g^{-1} after Fe$_3$O$_4$ particle loading.

3.3.4 XPS analysis. Considering XPS as more sensitive to the structural properties of nanostructured materials, the electron structures of the metal elements in Fe-HH-CGFS were further examined by XPS. As shown in Fig. 8a, the total spectrum proved the existence of C, O, Fe, and Si in Fe-HH-CGFS, and signified its high purity. The split peaks of the four elements C(1s), O(1s), Si(2p), and Fe(2p) in Fe-HH-CGFS were fitted, and the results are shown in Fig. 8b–e. The XPS spectra of C 1s for Fe-HH-CGFS included three component peaks at binding energies of 284.7, 285.5, and 288.9 eV (Fig. 8b), corresponding to the groups of C=C/C–C, C–O, and O–C=O.[48] From
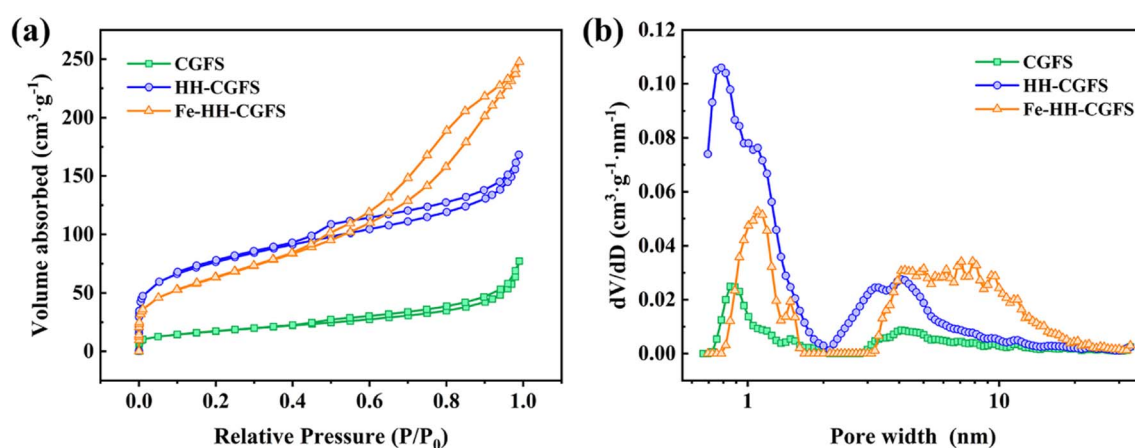

Fig. 7 (a) N$_2$ adsorption−desorption isotherms and (b) pore size distributions of CGFS, HH-CGFS, and Fe-HH-CGFS.
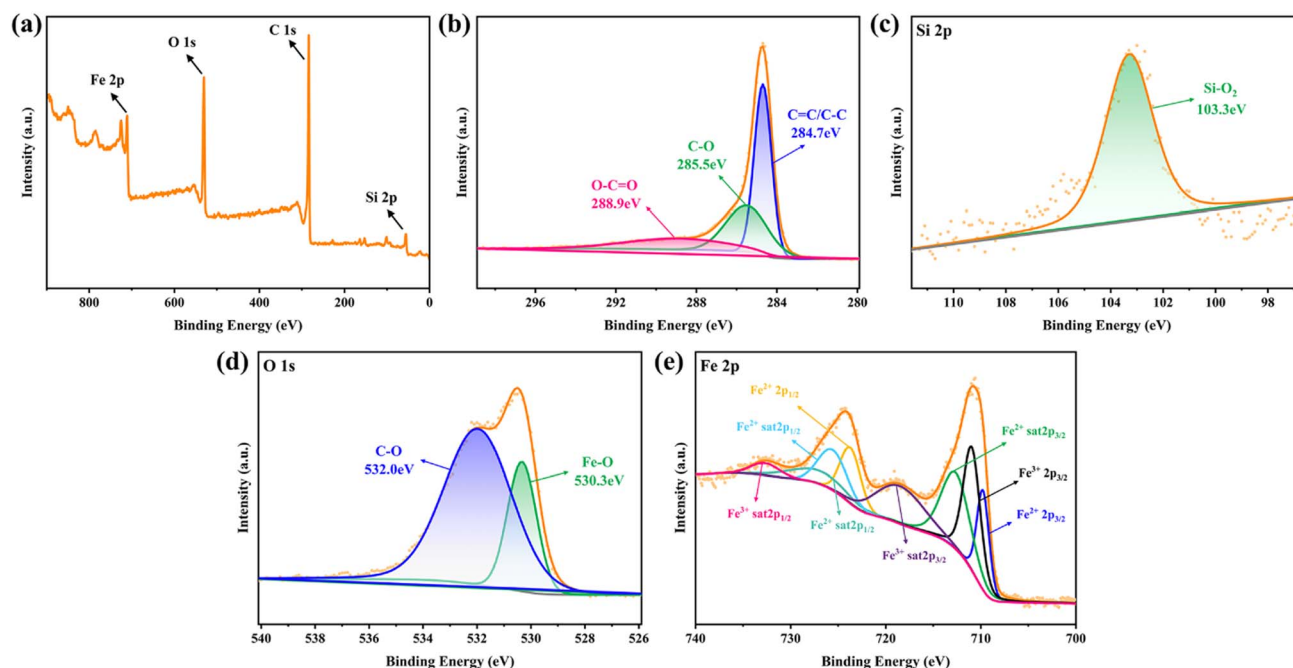

Fig. 8 XPS spectrograms of Fe-HH-CGFS: (a) the overall survey spectra, and high-resolution spectra of (b) C 1s, (c) Si 2p, (d) O 1s, and (e) Fe 2p.

the fitting results of Si 2p (Fig. 8c), it was proved that the predominant form of Si in Fe-HH-CGFS was $Si-O_2$ at 103.3 eV, with a possible trace amount of Si–O present. The O 1s spectrum can be split into two main peaks at 530.3 and 532.0 eV (Fig. 8d), thereby confirming the formation of magnetic Fe_3O_4 particles on the carbon skeleton of CGFS. In Fig. 8e, further analysis was performed to investigate the content of Fe^{3+} and Fe^{2+} and their ratios. The binding energies at 709.8 and 723.7 eV were derived from Fe^{2+} $2p_{3/2}$ and Fe^{2+} $2p_{1/2}$, which had two satellite peaks at the binding energies of 712.7 and 727.1 eV (Fe^{2+} sat $2p_{3/2}$ and Fe^{2+} sat $2p_{1/2}$). Similarly, there were two core level binding energies at 710.6 and 725.6 eV that correspond to Fe^{3+} $2p_{3/2}$ and Fe^{3+} $2p_{1/2}$ and were accompanied by two satellite peaks at the binding energies of 718.5 and 732.7 eV (Fe^{3+} sat $2p_{3/2}$ and Fe^{3+} sat $2p_{1/2}$).[48,49] The molar ratio of $Fe^{3+}:Fe^{2+}$ was calculated as 1 : 1.01 based on the peak areas, which was in good agreement with the molar ratio of $Fe^{3+}:Fe^{2+}$ (1 : 1) in the preparation of Fe-HH-CGFS.

3.3.5 TGA analysis. As shown in Fig. 9a, the TG curves of Fe-HH-CGFS showed two phases with the positions of the weight loss peaks at 42.4 °C and 550.4 °C, respectively. The first stage curve decreased flatly until 201.2 °C, which was due to the gradual loss of the crystalline water contained in the pores of Fe-HH-CGFS.[50,51] When the temperature reached between 447.7 and 627.2 °C, the TG curve loses weight significantly. This was attributed to the cleavage of the carbon chains and the structural collapse of Fe-HH-CGFS, which also involved a minor degree of metal hydrolysis cleavage, metal oxidation, and precipitation of volatile fractions. The broader peak shape observed in the second stage of the DTG curve further supports the prominent role of residual carbon combustion in Fe-HH-CGFS. After approximately 769.2 °C, the TG-DTG curve no longer changes, indicating complete combustion of the combustible material in Fe-HH-CGFS and termination of the reaction.

3.3.6 VSM analysis. The magnetic properties of Fe_3O_4 particles in Fe-HH-CGFS are largely influenced by their crystallinity and synthesis method.[52] The correlated saturation magnetization strength of Fe-HH-CGFS was measured by VSM (Fig. 9b) to be about 2.04 emu g^{-1}, making it suitable for solid–liquid separation in aqueous environments by magnetic attraction. Fe-HH-CGFS exhibited superparamagnetic behavior, as evidenced by their low coercivity (Hc) and residual
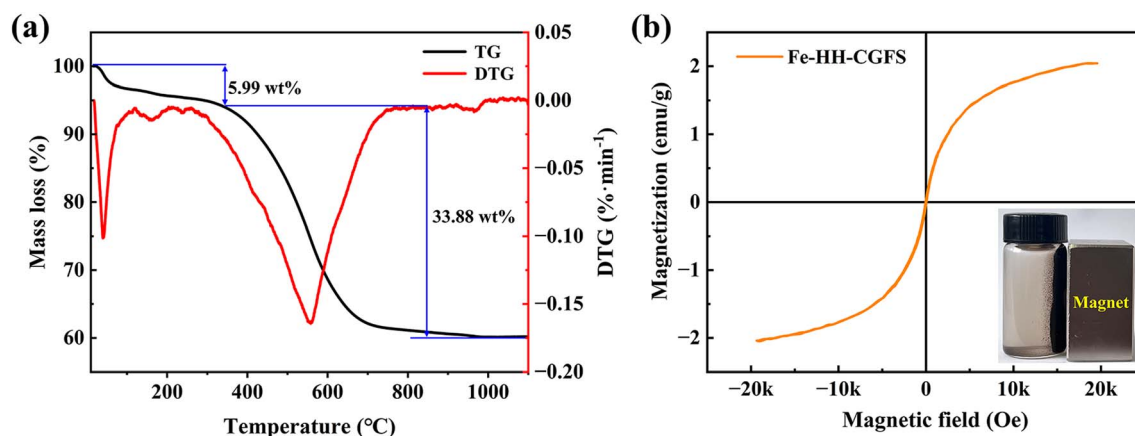

Fig. 9 (a) TG-DTG curves of Fe-HH-CGFS; (b) VSM hysteresis loops of Fe-HH-CGFS (inset is a photo of magnetic separation for Fe-HH-CGFS).
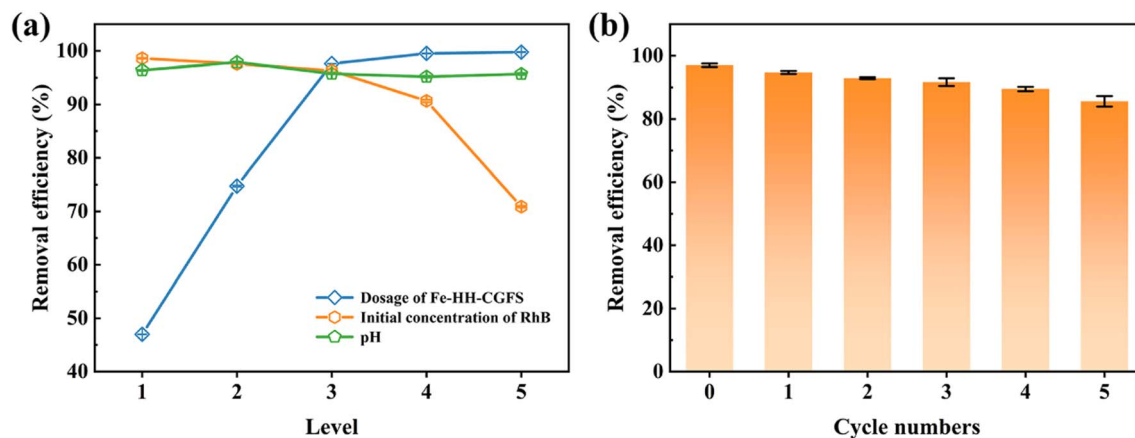

Fig. 10 (a) Effect of dosing amount, initial RhB concentration, and pH on the adsorption performance of Fe-HH-CGFS. (b) Reusability of Fe-HH-CGFS.

Table 2 Comparison of the maximum adsorption capacity of RhB on various adsorbents

| Adsorbent	Raw material	SSA (m^2 g^{-1})	Pore volume (cm^3 g^{-1})	q_m (mg g^{-1})	Ref.
sAC	Sawdust	1695		35.70	54
S@TP	Tapioca peel waste	146		33.10	55
Fly ash-based inorganic polymer	Fly ash	2.51	0.001037	21.99	56
LFO-ACFs	Fabric waste	7.39	0.0439	182.60	57
BHC-800	Bamboo shoot shells	513	0.27	85.80	58
HCF	Cassava slag	3.17		105.3	44
ST-1223-4h-1 to 2	Spent tyre	667		247	59
Fe-HH-CGFS	CGFS	196.84	0.346	188.68	This work
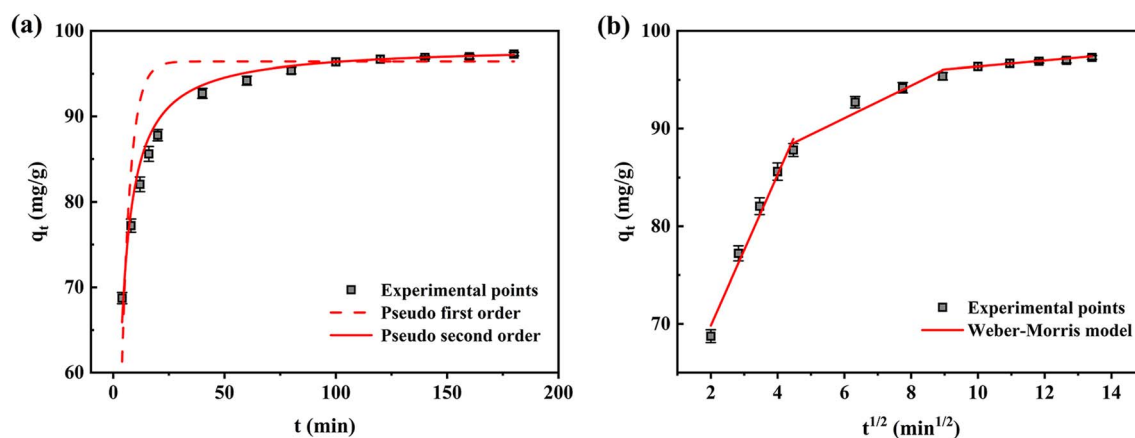
Fig. 11 Kinetics investigation on Fe-HH-CGFS. (a) PFO and PSO; (b) the Weber–Morris model.

magnetism (Mr), which ensured that Fe-HH-CGFS could be rapidly demagnetized upon removal of the magnetic field while maintaining good dispersion in solution.[53]

3.4 Adsorption performance investigations

3.4.1 Optimization of the operational conditions. As shown in Fig. 10a, the removal efficiency of RhB gradually increased from 46.99% to 99.75% when the dosage of Fe-HH-CGFS increased from 0.1 g L^{-1} to 2.0 g L^{-1}. These results could be attributed to the increased Fe-HH-CGFS providing sufficient adsorption sites to effectively remove most of the RhB in the solution, resulting in a higher removal efficiency. On the contrary, the removal efficiency of RhB decreased when its concentration increased from 50 mg L^{-1} to 200 mg L^{-1}. This phenomenon could be explained as follows: as the concentration increased, the amount of RhB molecules in the solution increased accordingly. However, due to the limited adsorption sites within the Fe-HH-CGFS pore channels, there was insufficient capacity to accommodate additional RhB molecules, reducing the removal efficiency. The optimum removal efficiency is achieved at a dosage of 1.0 g L^{-1}, and the initial concentration of RhB of 100 mg L^{-1}. It was further found that the effect of pH played a negligible role in the RhB removal efficiency, which reached a maximum of 97.90% at pH 5.0. These results revealed that Fe-HH-CGFS could be used as an effective adsorbent for RhB removal without deliberate pH adjustment in practical applications.[54] The optimal conditions were therefore optimized

as follows: the Fe-HH-CGFS dosage of 1.0 g L^{-1}, the initial concentration of RhB of 100 mg L^{-1}, and the pH of 5.0.

3.4.2 Stability evaluation of Fe-HH-CGFS. As shown in Fig. 10b, the adsorbed Fe-HH-CGFS was eluted with NaOH and then solid–liquid separated with a magnet, and the removal rate of RhB remained above 85% after five cycles of desorption–adsorption. The results revealed that Fe-HH-CGFS had good stability, leading to a higher removal efficiency of RhB.

A comparison of the effectiveness of Fe-HH-CGFS with other adsorbents previously reported in the literature for RhB is presented in Table 2. The findings suggested that Fe-HH-CGFS

Table 3 Kinetics analysis of Fe-HH-CGFS

Kinetics model	Q_e exp (mg g^{-1})	Q_e cal (mg g^{-1})	K_i (min^{-1})	R^2
PFO	97.4703	96.4167	0.2525	0.7689
PSO	97.4703	98.2483	0.0052	0.9838

Kinetics model		C_i (mg g^{-1})	K_{di} (mg g^{-1} min^{-1})	R^2
Weber–Morris model	Part I	54.3893	7.7226	0.9810
	Part II	81.0151	1.6739	0.9355
	Part III	93.3541	0.3001	0.9393

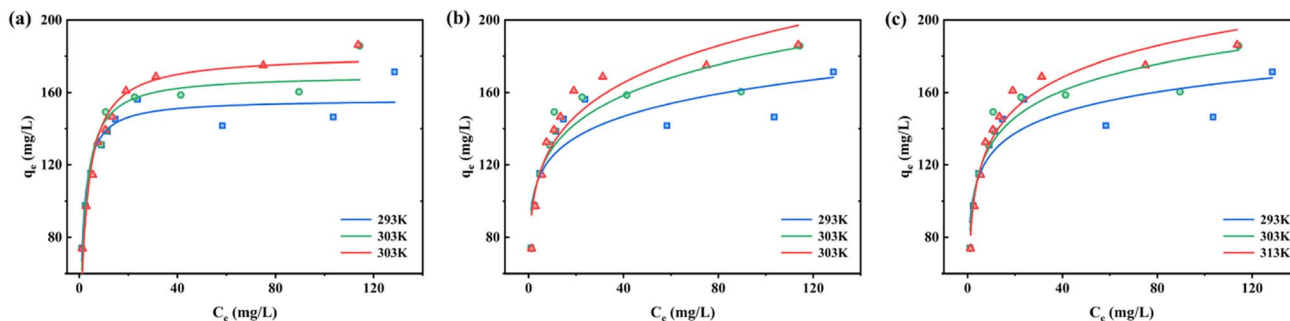© 2024 The Author(s). Published by the Royal Society of Chemistry

Fig. 12 Adsorption isotherms of RhB adsorption onto Fe-HH-CGFS. (a) Langmuir; (b) Freundlich; (c) Temkin.

exhibited significant potential for application in the treatment of RhB wastewater.

3.5 Adsorption mechanism investigation

3.5.1 Adsorption kinetics. PFO, PSO, and the Weber–Morris model were conducted to evaluate the adsorption kinetics in Fig. 11a and b. The parameters in Table 3 showed that the PSO model of Fe-HH-CGFS exhibited a higher R^2 value compared to the other two models, with an exceptional R^2 of 0.9838. The theoretical adsorption capacity of 98.25 mg L^{-1} obtained by calculation was close to the actual result of 97.47 mg L^{-1}, which proved the applicability of the PSO model. The PFO kinetic model assumed that the adsorption process was primarily controlled by the diffusion step, while the PSO theory suggested that the adsorption rate was mainly controlled by chemisorption.[58] Thus, the PSO model was more suitable to describe the adsorption process of RhB by Fe-HH-CGFS, suggesting that chemisorption was the dominant mechanism.[59,60] Furthermore, the Weber–Morris model showed that the adsorption process could be divided into three stages, and the

adsorption process of RhB on the outer surface of Fe-HH-CGFS occurred rapidly in the first stage, the mass transfer of RhB molecules within the pores of Fe-HH-CGFS took place in the second stage, and the adsorption process reached equilibrium in the third stage. Fig. 11b shows that none of the three fitted lines pass through the origin, indicating that the adsorption process involved both membrane diffusion and intra-particle diffusion.[61] Table 3 shows that the diffusion rate constants $K_{d1} > K_{d2} > K_{d3}$, indicating a rapid external mass transfer of RhB molecules during the adsorption process.

3.5.2 Adsorption isotherms. Adsorption experiments were carried out at the three temperatures of 293 K, 303 K, and 313 K (Fig. 12a–c). Firstly, the increase in RhB concentration helps to increase the adsorption of Fe-HH-CGFS, which is due to the increase in the driving force for mass transfer due to the increase in the solution concentration gradient.[62] Secondly, a higher temperature can also enhance the adsorption of RhB, which proves that the adsorption of RhB by Fe-HH-CGFS is an endothermic process. The fitted parameters of the three models are listed in Table 4. The Langmuir isotherm model was found to be more consistent with the experimental data, with a high correlation coefficient at all three temperatures. Finally, the adsorption of RhB onto Fe-HH-CGFS is a monolayer process that exhibits homogeneity. The potential energy of the adsorption sites remains constant throughout the process.

4. Conclusion

In this work, a novel magnetic carbon–silicon composite adsorbent Fe-HH-CGFS has been prepared *in situ* by a two-step acid leaching process and a one-step chemical co-precipitation. The following conclusions could be deduced.

(1) The results demonstrated that Fe-HH-CGFS exhibited a high SSA of 196.84 m² g⁻¹, excellent magnetic responsiveness with a saturation magnetization strength of 2.04 emu g⁻¹ based on BET and VSM analysis, and impressive performance with a maximum adsorption capacity for RhB of 97.69 mg g⁻¹ under the optimal conditions: an adsorbent dosage of 1.0 g L^{-1}, initial RhB concentration of 100 mg L^{-1}, and pH value of 5.0. The stability experiment revealed that the removal efficiency of RhB remained above 85% after undergoing five cycles.

(2) The RSM analysis based on BBD showed that the molar ratio of $Fe^{3+}:Fe^{2+}$ had a significant influence on the

Table 4 Kinetics analysis of Fe-HH-CGFS

Temperature (K)	Langmuir isotherm model		
	K_L (L mg⁻¹)	Q_{max} (mg L⁻¹)	R^2
293	0.7371	156.2305	0.9123
303	0.5343	169.8292	0.9266
313	0.3911	180.9089	0.9601
Temperature (K)	Freundlich isotherm model		
	K_F (mg g⁻¹)	n	R^2
293	95.0213	8.4854	0.7702
303	91.9234	6.7816	0.8683
313	89.0067	5.9537	0.9011
Temperature (K)	Temkin isotherm model		
	K_T (L mg⁻¹)	b	R^2
293	207.6775	16.4964	0.8242
303	47.5124	21.3122	0.9180
313	25.1392	20.2892	0.9564

morphology of the magnetic Fe_3O_4 nanoparticles and it was slightly affected by pH. Through analysis by SEM, XRD, XPS, BET, TGA, and VSM, it was found that the Fe_3O_4 particles synthesized with a molar ratio of $Fe^{3+} : Fe^{2+}$ of $1 : 1$ had a reverse spinel structure and were homogeneously dispersed on the carbon skeleton with an average particle size of 5.14 nm. The prepared Fe_3O_4 particles have excellent dispersion, small particle size, and high purity.

(3) The adsorption mechanisms revealed that the adsorption processes were in good agreement with the Langmuir isotherm model and the PSO model. The results indicated that the RhB removal process was a single-molecule layer endothermic adsorption, which is dominated by chemical adsorption reactions.

In summary, this work provides an alternative route for improving the additional value of the coal chemical industry and offers valuable insights into the preparation of magnetic carbon–silicon composites.

Conflicts of interest

There are no conflicts to declare.

Acknowledgements

References

1 Z. Xue, C. Yang, L. Dong, W. Bao, J. Wang and P. Fan, *Sep. Purif. Technol.*, 2023, **304**, 122394.

2 Y. Wang, Z. Zhang, L. Li, X. Guo, D. Wei, J. Kong, H. Du, H. Wang, Y. Zhuang and P. Xing, *J. Environ. Manage.*, 2023, **337**, 117681.

3 Z. Miao, J. Wu, Y. Niu, Z. Guo, F. Guo and Y. Zhang, *Chem. Eng. J.*, 2022, **435**, 134909.

4 D. Shi, J. Zhang, X. Hou, S. Li, H. Li, F. He and G. Zhu, *Fuel*, 2022, **323**, 124364.

5 J. Qu, J. Zhang, H. Li and S. Li, *Sci. Total Environ.*, 2021, **801**, 149761.

6 S. Gao, Y. Zhang, H. Li, J. He, H. Xu and C. Wu, *Fuel*, 2021, **290**, 120050.

7 Q. Guo, H. Li, S. Wang, Y. Gong, L. Ren and G. Yu, *Chem. Eng. J.*, 2022, **446**, 137256.

8 Y. Nie, Y. Jiang, Q. Wang, J. Chen, S. Wang and Q. Zhang, *J. Environ. Chem. Eng.*, 2023, **11**, 109934.

9 N. Yuan, A. Zhao, Z. Hu, K. Tan and J. Zhang, *Chemosphere*, 2022, **287**, 132227.

10 S. A. Haladu, *J. Mol. Liq.*, 2022, **357**, 119115.

11 R. Han, Y. Wang, Q. Sun, L. Wang, J. Song, X. He and C. Dou, *J. Hazard. Mater.*, 2010, **175**, 1056–1061.

12 L. Xu, K. Dong, F. Guo, S. Liu, Q. Qiao, S. Mao, L. Qian and Y. Bai, *Energy*, 2023, **274**, 127294.

13 W. Tang, H. Huang, Y. Gao, X. Liu, X. Yang, H. Ni and J. Zhang, *Mater. Des.*, 2015, **88**, 1191–1200.

14 Z. Miao, J. Wu, G. Qiu, Z. Guo, X. Zhao and Y. Zhang, *Sci. Total Environ.*, 2022, **821**, 153347.

15 X. Ma, Y. Li, D. Xu, H. Tian and H. Yang, *J. Environ. Manage.*, 2022, **305**, 114404.

16 D. Zhu, J. Zuo, Y. Jiang, J. Zhang, J. Zhang and C. Wei, *Sci. Total Environ.*, 2020, **707**, 136102.

17 Z. Miao, F. Guo, X. Zhao, Z. Guo, Y. Guo, Y. Zhang and J. Wu, *Chem. Eng. Res. Des.*, 2021, **169**, 1–8.

18 F. S. A. Khan, N. M. Mubarak, Y. H. Tan, M. Khalid, R. R. Karri, R. Walvekar, E. C. Abdullah, S. Nizamuddin and S. A. Mazari, *J. Hazard. Mater.*, 2021, **413**, 125375.

19 T. A. Saleh, S. H. Al-Ruwayshid, A. Sarı and M. Tuzen, *Eur. Polym. J.*, 2020, **130**, 109698.

20 H. He, Z. Luo and C. Yu, *J. Alloys Compd.*, 2020, **816**, 152652.

21 S. Gao, H. Xing, J. Zhang, Y. Liu, H. Du, Z. Zhu, J. Wang, X. Li, S. Zhang, Y. Yao and L. Ren, *J. Materiomics*, 2021, 7, 1275–1283.

22 M. Berkani, Y. Kadmi, M. K. Bouchareb, M. Bouhelassa and A. Bouzaza, *Arabian J. Chem.*, 2020, **13**, 8338–8346.

23 S. L. Ferreira, R. E. Bruns, H. S. Ferreira, G. D. Matos, J. M. David, G. C. Brandao, E. G. da Silva, L. A. Portugal, P. S. dos Reis, A. S. Souza and W. N. dos Santos, *Anal. Chim. Acta*, 2007, **597**, 179–186.

24 N. Aslan and Y. Cebeci, *Fuel*, 2007, **86**, 90–97.

25 T. Li, S. He, T. Shen, J. Sun, C. Sun, H. Pan, D. Yu, W. Lu, R. Li, E. Zhang, X. Lu, Y. Fan and G. Gao, *Int. J. Environ. Res. Public Health*, 2022, **19**, 12851.

26 S. He, T. Li, T. Shen, J. Sun, H. Pan, C. Sun, W. Lu, X. Lu, G. Gao, Y. Fan, R. Li, E. Zhang and D. Yu, *Process Saf. Environ. Prot.*, 2023, **173**, 249–262.

27 S. Liu, X. Chen, W. Ai and C. Wei, *J. Cleaner Prod.*, 2019, **212**, 1062–1071.

28 C.-C. Lin and J.-M. Ho, *Ceram. Int.*, 2014, **40**, 10275–10282.

29 H. Meng, Z. Zhang, F. Zhao, T. Qiu and J. Yang, *Appl. Surf. Sci.*, 2013, **280**, 679–685.

30 L. Jun, D. Runan, W. Yi, H. Jiannan, H. Shuang and S. Jianping, *Shenyang Jianzhu Daxue Xuebao, Ziran Kexueban*, 2017, **33**, 378–384.

31 Z. J. Zhang, J. Ma, S. B. Xu, J. H. Ren, Y. Qin, J. Huang, K. Y. Yang, Z. P. Zhang and G. Wu, *J. Huazhong Univ. Sci. Technol., Med. Sci.*, 2014, **34**, 270–275.

32 Z.-r. Zhang, S.-h. Luo, J.-c. Wang, M.-y. Sun, S.-x. Yan, Q. Wang, Y.-h. Zhang, X. Liu and X.-f. Lei, *J. Energy Storage*, 2022, **56**, 105913.

33 D. T. C. Nguyen and T. V. Tran, *Chem. Pap.*, 2022, **76**, 4873–4883.

34 H. V. Tran, N. M. Ngo, R. Medhi, P. Srinoi, T. Liu, S. Rittikulsittichai and T. R. Lee, *Materials*, 2022, **15**, 503.

35 P. Liu, T. Wang, Z. Yang, Y. Hong, X. Xie and Y. Hou, *Sci. Total Environ.*, 2020, **704**, 135286.

36 Y. Yao, S. Miao, S. Liu, L. P. Ma, H. Sun and S. Wang, *Chem. Eng. J.*, 2012, **184**, 326–332.

37 S. Rajput, C. U. Pittman, Jr. and D. Mohan, *J. Colloid Interface Sci.*, 2016, **468**, 334–346.

38 L. Lu, N. Liang, H. Sun, Q. Zhang and X. Hao, *J. Materiomics*, 2022, **8**, 47–58.

39 B. Yang, Q. Zhang, X. Ma, J. Kang, J. Shi and B. Tang, *Nano Res.*, 2016, **9**, 1879–1890.

40 P. Liu, Z. Yao, V. M. H. Ng, J. Zhou, L. B. Kong and K. Yue, *Composites, Part A*, 2018, **115**, 371–382.

41 P. Liu, V. M. H. Ng, Z. Yao, J. Zhou and L. B. Kong, *Mater. Lett.*, 2018, **229**, 286–289.

42 B. Li, J. Ma, L. Zhou and Y. Qiu, *Chem. Eng. J.*, 2017, **330**, 191–201.

43 H. G. Jiang, M. Rühle and E. J. Lavernia, *J. Mater. Res.*, 1999, **14**, 549–559.

44 Y. Zhang, X. Cao, G. Wu, J. Wang and T. Zhang, *Appl. Surf. Sci.*, 2020, **527**, 146803.

45 C. Kang, D. Shang, T. Yang, L. Zhu, F. Liu, N. Wang and T. Tian, *Chem. Res. Chin. Univ.*, 2018, **34**, 1014–1019.

46 X. Ma, L. Yang, Y. Hou and L. Zhou, *J. Environ. Manage.*, 2022, **305**, 114360.

47 N. Pan, S. Liu, Y. Han, D. Li and J. Chai, *J. Materiomics*, 2022, **8**, 781–789.

48 J. He, S. Gao, Y. Zhang and H. Li, *J. Alloys Compd.*, 2021, **874**, 159878.

49 M. Ren, F. Li, B. Wang, J. Wei and Q. Yu, *J. Magn. Magn. Mater.*, 2020, **513**, 167259.

50 J. Ma, R. Zhang, W. Xia, Y. Kong, Y. Nie, Y. Zhou and C. Zhang, *Sep. Purif. Technol.*, 2022, **285**, 124401.

51 Z. Chai, B. Liu, P. Lv, Y. Bai, J. Wang, X. Song, W. Su and G. Yu, *Fuel*, 2023, **333**, 126318.

52 P. Hu, S. Zhang, H. Wang, D. a. Pan, J. Tian, Z. Tang and A. A. Volinsky, *J. Alloys Compd.*, 2011, **509**, 2316–2319.

53 J. Chen, S. Lin and J. Yu, *J. Hazard. Mater.*, 2020, **388**, 122101.

54 V. H. Nguyen, D. T. Nguyen, T. T. Nguyen, H. P. T. Nguyen, H. B. Khuat, T. H. Nguyen, V. K. Tran, S. Woong Chang, P. Nguyen-Tri, D. D. Nguyen and D. D. La, *Environ. Technol. Innovation*, 2021, **24**, 101801.

55 S. Vigneshwaran, P. Sirajudheen, P. Karthikeyan and S. Meenakshi, *Surf. Interfaces*, 2021, **23**, 100920.

56 M. El Alouani, S. Alehyen, H. El Hadki, H. Saufi, A. Elhalil, O. K. Kabbaj and M. h. Taibi, *Surf. Interfaces*, 2021, **24**, 101136.

57 Y. Hou, G. Huang, J. Li, Q. Yang, S. Huang and J. Cai, *J. Anal. Appl. Pyrolysis*, 2019, **143**, 104694.

58 M. Y. Nassar, E. A. Abdelrahman, A. A. Aly and T. Y. Mohamed, *J. Mol. Liq.*, 2017, **248**, 302–313.

59 J. Zhang, M. Zhu, I. Jones, Z. Zhang, J. Gao and D. Zhang, *Environ. Sci. Pollut. Res. Int.*, 2021, **28**, 52862–52872.

60 Q. Qiao, H. Zhou, F. Guo, R. Shu, S. Liu, L. Xu, K. Dong and Y. Bai, *J. Cleaner Prod.*, 2022, **379**, 134739.

61 B. Liu, Z. Chai, P. Lv, Y. Bai, J. Wang, Q. Guo, W. Su and G. Yu, *Fuel*, 2023, **128318**, 346–359.

62 R. Shu, Q. Qiao, F. Guo, K. Dong, S. Liu, L. Xu, Y. Bai and N. Zhou, *Environ. Res.*, 2023, **217**, 114912.